Rae Auriol, S. P. (Orcid ID: 0000-0003-3420-4135)
Kenkmann Thomas (Orcid ID: 0000-0002-8127-6812)

Dynamic Compressive Strength and Fragmentation in Felsic Crystalline Rocks

Auriol S. P. Rae[1,2], Thomas Kenkmann[1], Vivek Padmanabha[1,3], Michael H. Poelchau[1], Frank Schäfer[1,3]

[1]Institute of Earth and Environmental Sciences – Geology, Albert-Ludwigs Universität Freiburg, Albertstrasse 23b, 79104 Freiburg, Germany.

[2]Department of Earth Sciences, University of Cambridge, Cambridge CB2 3EQ, UK

[3]Fraunhofer Ernst-Mach-Institute, Eckerstrasse 4, 79104 Freiburg, Germany.

Corresponding author: Auriol S. P. Rae (auriol.rae@geologie.uni-freiburg.de)

Key Points:

- The strength of felsic crystalline rocks significantly increases beyond transition strain rates of ~22.9 s^{-1}.
- Fragment sizes from compressive failure are related to strain-rate by a power-law that is inconsistent with current fragmentation models.
- Dynamic strength and fragmentation of rocks may be important processes during impact cratering and other fast geohazards.

This article has been accepted for publication and undergone full peer review but has not been through the copyediting, typesetting, pagination and proofreading process which may lead to differences between this version and the Version of Record. Please cite this article as doi: 10.1029/2020JE006561

Abstract

Brittle deformation in rocks depends upon loading rate; with increasing rates, typically greater than ~10^2 s^{-1}, rocks become significantly stronger and undergo increasingly severe fragmentation. Dynamic conditions required for rate-dependent brittle failure may be reached during impact events, seismogenic rupture, and landslides. Material characteristics and fragment characterization of specific geomaterials from dynamic loading are only approximately known. Here we determine the characteristic strain rate for dynamic behavior in felsic crystalline rocks, including anisotropy, and describe the resulting fragments. Regardless of the type of felsic crystalline rock or anisotropy, the characteristic strain rate is the same within uncertainties for all tested materials, with an average value of 229 ± 81 s^{-1}. Despite the lack of variation of the critical strain rate with lithology, we find that the degree of fragmentation as a function of strain rate varies depending on material. Scaled or not, the fragmentation results are inconsistent with current theoretical models of fragmentation. Additionally, we demonstrate that conditions during impact cratering, where the impactor diameter is less than ~100 m, are analogous to the experiments carried out here, and therefore that dynamic strengthening and compressive fragmentation should be considered as important processes during impact cratering.

Plain Language Summary

When rocks deform quickly, they can behave with properties very different to the properties that would be measured when rocks are deformed slowly. In this study, we have measured the strength of rocks deformed at different rates to find how fast they must be deformed to cause substantial changes to their properties. We chose to look at granitic rocks and gneisses as they are broadly representative of the Earth's continental crust. We found that regardless of the exact rock type, the change from slow to fast deformation occurs at the same rate. When rocks break at fast rates, they break into many small fragments. We have measured the size of those fragments from our experiments to show how the average fragment size changes as a result of the deformation rate and the rock type. In addition, we show that the changes of properties that we see in our experiments is important for the formation of impact craters and potentially earthquake rupture and landslides.

1 Introduction

Rock strength and fragmentation during dynamic deformation is critically controlled by strain rate (Aben et al., 2017; Ramesh et al., 2015). Dynamic deformation occurs in a variety of planetary and geological processes: hypervelocity impact (Kenkmann et al., 2014), seismogenic ruptures (Doan and Gary, 2009), and landslides (McSaveney and Davies, 2006). During dynamic loading, brittle materials such as rocks have higher yield strengths (e.g. (Zwiessler et al., 2017)) and potentially variable elastic moduli (see (Zhang and Zhao, 2014)) in comparison to quasi-static loading. In failure, increased loading-rates result in increased fragmentation of the material and may cause rock pulverization (Aben et al., 2016; Barber and Griffith, 2017; Doan and Gary, 2009; Ghaffari et al., 2019; Yao et al., 2020; Yuan et al., 2011). Changes in material properties and fragmentation are the result of the behavior of fractures. Fractures propagate at a finite velocity; at high loading rates, the weakest flaws in a material are not able to cause failure before other, increasingly strong flaws are activated (Aben et al., 2017; Ramesh et al., 2015).

Rock strength can be investigated over a range of strain rate regimes (Zhang and Zhao, 2014): quasi-static (10^{-5} – 10^{-1} s^{-1}), intermediate strain rate (10^{-1} – 10^{1} s^{-1}), high strain rate (10^{1} – 10^{4} s^{-1}), and very high strain rate (>10^{4} s^{-1}). Results across those regimes (Aben et al., 2017; Ramesh et al., 2015) demonstrate that rocks behave with a strength that is near-constant at quasi-static rates and increases markedly beyond a threshold strain rate in the intermediate to high strain rate regime. Experiments at very high strain rates show that strength becomes independent of rate. Micro-mechanical models (Paliwal and Ramesh, 2008) demonstrate that the behavior of the compressive strength of rocks from quasi-static to high strain rates can be described by a universal scaling relationship (Kimberley et al., 2013):

$$\frac{\sigma_c}{\sigma_0} = 1 + \frac{\dot{\varepsilon}}{\dot{\varepsilon}_0}^{2/3}, \textbf{(1)}$$

where σ_c and $\dot{\varepsilon}$ are the unconfined compressive strength and strain rate respectively. The parameters σ_0 and $\dot{\varepsilon}_0$ are the characteristic stress and characteristic strain rate for the material. The characteristic stress is equivalent to the quasi-static uniaxial compressive strength, while the characteristic strain rate is the rate at which the dynamic strength is twice the value of the quasi-static uniaxial compressive strength. Strength becomes significantly different to the quasi-static uniaxial compressive strength above a rate known as the "transition strain rate", which can be defined as one tenth of the characteristic strain rate. In the theoretical formulation by (Kimberley et al., 2013), the characteristic stress and strain rate are determined from

material and microstructural properties: fracture toughness, elastic modulus, wave speed, flaw size, and flaw density. The theoretically derived relationship is consistent with a variety of experimental results across a wide range of strain rates.

The dependency of material strength on strain is fundamentally linked to the behavior and activation of fractures and the production of fragments (Aben et al., 2017; Ramesh et al., 2015). At low rates, failure is accommodated by widely spaced, localized fractures. Higher rates lead to increasingly pervasive fracturing and fragmentation (Doan and Gary, 2009; Yao et al., 2020; Yuan et al., 2011). As a consequence, energy dissipation and the energy budget between fracture energy and the kinetic energy of fragments is significantly affected by strain rate (Barber and Griffith, 2017; Ghaffari et al., 2019). Thus, predicting the number, size, and shape distributions of fragments is a critical component to any model that aims to describe dynamic brittle failure (Grady, 2009). Dynamic fragmentation is extremely complex and there is currently no generally accepted theory of fragmentation, including consensus on the type of distribution that best represents the statistical nature of fragment size distributions (see (Grady, 2009)). Nevertheless, analytical and numerical models have been developed to predict average fragment size and distributions for specific applications (Glenn and Chudnovsky, 1986; Grady, 1982; Levy and Molinari, 2010; Zhou et al., 2006a, 2006b).

The fragmentation of an expanding ring, first described and analyzed by (Mott, 1947, 1943), is one of the longest standing and most commonly modelled problems in dynamic fracture mechanics. By an energy balance approach where all local kinetic energy is converted into fracture energy, (Grady, 1982) derived a relationship to predict the average fragment size. He predicted that the average fragment size was proportional to strain rate by a power law with an exponent of $-2/3$. (Glenn and Chudnovsky, 1986) extended the work by Grady to include the contribution from elastic potential energy, resulting in the prediction of a quasi-static fragment size independent of strain rate, but the same dependence of fragment size on strain rate at high rates. More recently, (Zhou et al., 2006a, 2006b) and (Levy and Molinari, 2010) developed parameterizations to predict the dominant fragment size based on the results of numerical simulations. Those parameterizations have a broadly similar shape to the model of (Glenn and Chudnovsky, 1986) and have the same dependence of fragment size on strain rate at high rates.

Fracturing and fragmentation in an expanding ring is a tensile process. Nevertheless, several workers have attempted to compare unconfined compressive failure of brittle materials

using hydraulic presses, drop-weight apparatus, and split-Hopkinson pressure bars (Ghaffari et al., 2019; Hogan et al., 2013, 2012; Lankford and Blanchard, 1991; Wang and Ramesh, 2004). Results from these experiments have suggested that the models of (Grady, 1982) and (Glenn and Chudnovsky, 1986) over-estimate the average fragment size. More recently though, it has been recognized (Hogan et al., 2016; Ramesh et al., 2015) that comparison between experiments of compressive fragmentation and currently existing tensile fragmentation models should not be made directly and require scaling the compressive strain rate to an equivalent tensile strain rate.

In this contribution, we aim to investigate the dynamic behavior of rocks in compressive failure, more specifically we have chosen to investigate lithologies that are broadly representative of the earth's continental crust, felsic crystalline rocks, due to their relevance to impact cratering (e.g. (Kenkmann et al., 2014)), earthquake rupture (e.g. (Doan and Gary, 2009)), landslides (e.g. (Davies and McSaveney, 2009)), and other dynamic geoprocesses. Additionally, we investigate the effect of fabric anisotropy in rocks during dynamic compression. In order to investigate the dynamic failure of these rocks, we have conducted rock mechanical experiments at a variety of strain rates and investigated the products of that failure by analyzing their fragment size distributions.

2 Methods

2.1 Material Description

To address the aims of our study, we chose to study a granite and a gneiss. Blocks of Granite, hereafter termed 'Malsburg Granite', were acquired from Alfred Dörflinger GmbH, near Malsburg, Black Forest, Germany. Blocks of Gneiss, hereafter termed 'Maggia Gneiss', were acquired from Sud Nord Graniti SA in Valle Maggia, Switzerland. The Malsburg Granite is composed of ~38% plagioclase feldspar, ~22% quartz, ~26% alkali feldspar, ~13% biotite, and ~ 1% hornblende (Hahn-Weinheimer and Ackermann, 1967). The felsic major minerals are typically 1-2 mm in size, while occasional ~5 mm phenocrysts of plagioclase occur. The mafic major minerals are <1 mm in size. The granite has no preferred fabric and is isotropic. The bulk density and porosity of the Malsburg Granite was determined by He-pycnometry to be 2623 ± 4 kg m^{-3} and 0.29 ± 0.02 % respectively. The Maggia Gneiss is composed of ~50% plagioclase feldspar, ~40% biotite, ~8% quartz, and 2% accessory phases, including pyroxene, muscovite, epidote, and apatite (Agarwal et al., 2019). The grain sizes of the major mineral

phases are approximately 0.5-2 mm. The grains of biotite are aligned to form a strong foliation through the lithology, causing transversely isotropic mechanical behavior. The foliation has a spacing of approximately 1-2 mm, although occasional leucocratic bands can be up to 5 mm in thickness. The bulk density and porosity of the Maggia Gneiss was determined by He-pycnometry to be 2745 ± 14 kg m^{-3} and 0.46 ± 0.01 % respectively.

The samples used for rock deformation experiments were cored from the blocks of Maggia Gneiss and Malsburg Granite. In the case of Maggia Gneiss cores, plugs were taken parallel and perpendicular to the foliation. Typical samples were ~41 mm in diameter, although some samples were of different diameters to more easily facilitate failure under high-rate conditions. The length of the samples, and by consequence, aspect ratio, were changed for the different experimental apparatus used. Both lithologies are medium-grained, with grains substantially smaller than the sample size. However, there are occasional large phenocrysts within the Malsburg Granite and wide leucocratic foliations in the Maggia Gneiss, both can measure on a scale up to ~12% of the sample diameter. As a consequence, some scatter of the experimental results is to be expected. A total of 25 experiments were carried out on the Malsburg Granite, and 57 experiments were carried out on the Maggia Gneiss. Of the Maggia Gneiss experiments, 24 were conducted where the foliation was parallel to the compression axis and 33 were conducted where the foliation was perpendicular to the compression axis.

2.2 Experimental Rock Deformation

Rock mechanical experiments were carried out in three suites: first, the Malsburg Granite; second, the Maggia Gneiss where the foliation was parallel to the compression axis; and third, the Maggia Gneiss where the foliation was perpendicular to the compression axis. Both orientations of the Maggia Gneiss were required due to the anisotropy (transverse isotropy) of the material.

Quasi-static uniaxial compression experiments were performed with a servo-controlled Form+Test Alpha 2-3000 S hydraulic press at the Geology Department of the University of Freiburg. Displacement gauges were used to measure both the longitudinal strain and transverse strain in the samples, enabling measurement of the elastic moduli and Poisson's ratio of the lithologies. Experiments were run under constant force-loading conditions, resulting in constant strain rates in the elastic regime and an increase in strain rate immediately before failure. Experiments in this study were run at strain rates (in the elastic regime) between 4.9 ×

10^{-6} and 1.0×10^{-5} s^{-1}. At least 5 quasi-static experiments were carried out for each experimental suite. Samples for quasi-static uniaxial compression experiments all had a length-to-diameter ratio of 2:1.

Dynamic uniaxial compression experiments were performed with a split Hopkinson pressure bar (SHPB) at the Geology Department of the University of Freiburg. A SHPB consists of three units; a striker, an incident bar, and a transmission bar. The sample is placed between the incident and transmission bars. A stress wave is generated by the collision of the striker with the incident bar. The stress wave propagates through the incident bar, sample, and transmission bar causing deformation to the sample. The stress and strain history of all SHPB experiments were calculated from the signals of strain gauges attached to the incident and transmission bars (see **Supplementary Text 1** for details), without any direct measurement of strain from strain gauges on the sample or from digital image correlation. The SHPB experiments in this study reached strain rates between 16.9 and 322.8 s^{-1}. The samples used in the experiments in this study typically had a length-to-diameter ratio of 1:1. A detailed description of the methodology of the SHPB in this study is provided in **Supplementary Text 1**. General descriptions of the methodology of SHPBs can be found in (Aben et al., 2017; Chen and Song, 2010; Xia and Yao, 2015; Zhang and Zhao, 2014; Zwiessler et al., 2017).

2.3 Fragment Size Analysis

There are two common ways to represent fragment size distributions: number-size distributions and mass-size distributions. Number-size distributions follow from counting and measuring each individual fragment. Mass-size distributions follow from weighing all fragments within specified size ranges using sieving and/or other techniques. In this study, we represent all fragment size distributions using mass-size distributions, obtained by sieving of the rock fragments resulting from the experiments. Sieve sizes used in our analysis were 0.2, 0.4, 0.63, 1, 2, 6.3, and 16 mm. We found that none of the samples had more than 10.1 % of the total mass less than 0.2 mm, and thus all of the fragment size distributions were well characterized within the range of sieve sizes.

Fragment size distributions can be statistically treated in a variety of ways (see (Grady, 2010)). Notably, a variety of statistical distributions can be used to fit fragment size distributions. In this study, we chose to fit our data to cumulative Weibull distributions:

$$\frac{M(s)}{M_T} = 1 - \exp\left[-\left(\frac{s}{\lambda}\right)^k\right], \textbf{(2)}$$

where $M(s)$ is the cumulative mass of fragments that have a size less than s; M_T is the total sample mass; and λ and k are the scale and shape parameters of the distribution respectively. We note that many other distributions could have been used to fit our fragment size data, e.g., Rayleigh (Levy and Molinari, 2010), log-normal (Wang and Ramesh, 2004), or generalized extreme value (Hogan et al., 2012). However, we chose to use Weibull distributions here as they are mathematically simple, provide a reasonable fit to our data, and have easily definable average values. The median of a Weibull distribution, $\bar{s}$, can be calculated as:

$$\bar{s} = \lambda \ln(2)^{1/k}. \textbf{(3)}$$

$\bar{s}$ is the size of fragment that equally divides the mass contribution of the large fragments from the mass contribution of the small fragments. This size is larger than the median fragment size from a number-size distribution, if it were possible to determine that distribution. Here we use it as the "average fragment size".

An additional advantage of using Weibull distributions to fit our data is that at small values of the independent variable, it reduces to a power law (Turcotte, 1986), a potentially important characteristic of fragment size distributions of brittle materials as it implies scale-invariance (Grady, 2010). Power law fragment distributions are commonly defined as number-size distributions:

$$N(s) \sim s^{-D}, \textbf{(4)}$$

where $N(s)$ is the number of fragments with a size greater than s. D is the so-called "fractal dimension" or "D-value". Where $s \ll \lambda$, D can be determined and is related to the shape parameter of the Weibull distribution:

$$D = 3 - k, \textbf{(5)}$$

D cannot be evaluated where k > 3. Distributions of this type are heavily skewed towards small numbers of large particles, i.e. a sample that has split into a few countable fragments, where the distribution is non-fractal.

3 Results

A summary of all the experiments in this study can be found in the **Supplementary Online Data Set** (Rae et al., 2020).

3.1 Mechanical Data

In general, results show that the experiments at higher strain rates have larger failure strengths (**Figure 1**). For the same strain rate, the Malsburg granite has the lowest stress at failure for each of the three experimental suites, while the Maggia Gneiss (perpendicular) has the largest stress at failure. The SHPB experiments appear to accumulate large amounts of strain at low stress, producing a concave-upwards shape to the stress-strain relationships at low stresses. We do not believe these correspond to the behavior of the sample material, instead, it is likely to be caused by the compaction of silicone grease, titanium plates, Teflon sheets, and potentially trapped air between the bar ends and the sample. In separate tests, we found that this compaction accounted for ~0.12 mm of displacement. An additional cause of the concave-upwards shape of the stress-strain relationship at low stresses may derive from the pulse-shaper or picking of the incident wave in data processing.

The failure stresses (i.e. strength) of the three suites of experimental data are consistent, despite some scatter, with the scaling law of (Kimberley et al., 2013) (**Figure 2**). Scatter in the data are likely to be a result of heterogeneities such as large phenocrysts and/or foliations. We note that the experimental data could be fitted by a number of other numerical relationships, however, none of these would have a theoretical grounding in the micromechanics of fracture growth. The values of characteristic (quasi-static) strength and strain rate for each experimental suite were determined by non-linear least squares fitting of the data to **Equation 1**, providing values and 1 standard deviation uncertainties for the parameters (**Table 1**). The quasi-static strengths, σ_0, of the Malsburg Granite, Maggia Gneiss (parallel), and Maggia Gneiss (perpendicular) are 128.0 ± 17.7 MPa, 149.5 ± 11.7 MPa, and 181.3 ± 12.6 MPa, respectively. The Maggia Gneiss is therefore 21% stronger when compressed perpendicular to the foliation. While the three sample suites have different quasi-static strengths, the characteristic strain rates $\dot{\varepsilon}_0$ that control the dependency of strength on strain rate are 215 ± 93 s^{-1}, 234 ± 79 s^{-1}, and 238 ± 65 s^{-1}, respectively. These values are all within uncertainty of each other. These characteristic rates correspond to the strain rate at which strength is double the quasi-static strength. The transition strain rates ($\sim \dot{\varepsilon}_0/10$), defining the strain rate beyond which strength becomes

significantly rate-dependent (Kimberley et al., 2013), are 21.5 ± 9.3 s^{-1}, 23.4 ± 7.9 s^{-1}, and 23.8 ± 6.5 s^{-1}, respectively (**Table 1**).

Quasi-static values for the elastic modulus of the Marlsburg Granite and Maggia Gneiss (parallel and perpendicular) are 36.1 ± 1.5 GPa, 39.0 ± 4.9 GPa, and 33.0 ± 2.0 GPa, respectively (**Table 1**). Thus, the Maggia Gneiss is stiffer but weaker when compressed parallel to the foliation than perpendicular to the foliation. There is no clear relationship between strain rate and the elastic modulus (**Figure 3**). However, the average elastic modulus from SHPB experiments of the Malsburg Granite and Maggia Gneiss (parallel) are 24.3 ± 6.9 GPa and 29.1 ± 7.0 GPa, less than the quasi-static elastic moduli of those materials and with much greater scatter. Meanwhile, for the Maggia Gneiss (perpendicular) the average elastic modulus from SHPB experiments is 36.4 ± 7.6 GPa, similar to the quasi-static elastic modulus but with much greater scatter.

3.2 Fragment Size Distributions

Samples deformed at high strain rates result in a larger number of fragments than samples deformed at lower strain rates. Fragment size distributions for all of the failed SHPB samples are shown in **Figure 4**. At low strain rates, only a small fraction of the sample progresses beyond the largest sieve, i.e. almost all of the mass of the sample is contributed by fragments larger than 16 mm, but smaller than the sample size (typically ~40 mm). In the samples deformed at the highest strain rates, large mass contributions are made by fragments in all bin sizes, spanning two orders of magnitude.

The progression of fragment size distributions with strain rate can be seen in the progression of median fragment size, as determined from from the mass-size distributions, with strain rate (**Figure 5a**), strain rate is related to fragment size by a power law, $\bar{s} \sim \dot{\varepsilon}^N$, for all three experimental suites. The exponent of those power laws, N, for the Malsburg Granite and Maggia Gneiss (Parallel) are similar, -1.52 ± 0.10 and -1.31 ± 0.08, although the exponent for the Malsburg greater is slightly more negative. However, the Maggia Gneiss (perpendicular) has a distinctly different exponent, -2.23 ± 0.21. In addition to the progression of fragment size with strain rate, the fractal dimension, D, of the fragment size distributions (**Equation 5**) varies with increasing strain rate. All materials follow the same trend where at rates below 150 s^{-1}, D-values increase rapidly with increasing strain rate; above ~150 s^{-1}, D-values gradually and

linearly increase from a value of ~1.95, up to ~2.15 at rates of ~300 s^{-1} (**Figure 5b**). This result is broadly consistent with (Barber and Griffith, 2017), who measured 2.65 < D < 3.14 at rates from 931 – 1154 s^{-1}.

During dynamic brittle failure, fragments can be ejected with substantial kinetic energy, and capturing all of the fragments can be challenging (e.g. (Barber and Griffith, 2017)). Although we attempted to completely recover the fragments from each experiment, we recovered an average of 93.4% of the total mass of each sample, ranging from 97.8% down to 82.2%. Sample recovery was generally worse with increasing strain rate/ fragmentation of the sample, suggesting that fine fragments (< ~1 mm) are more commonly lost than larger fragments. The effect of this on our results is that high strain rates may result in smaller median particle sizes and larger D-values (**Figure 5**), although we note that this effect is likely to be small as the proportion of fine particles in all of the distributions, with the exception of two samples of Malsburg Granite, always less than a third of the total mass.

In summary, the foliation within the Maggia Gneiss has a significant effect on mechanical properties and fragmentation. The material is stiffer and weaker when loaded parallel to the foliation. Despite these differences, the characteristic strain rate for rate dependency is independent of the orientation of the foliation. A summary of results can be found in **Table 1**.

4 Discussion

The quasi-static strengths of the lithologies used in this study are broadly typical for crystalline felsic rocks (Green et al., 1972; Kumar, 1968; Perkins et al., 1970; Yuan et al., 2011). Under dynamic testing conditions the strain rate beyond which dynamic strength is significant has only been approximately estimated for crystalline felsic rocks. (Blanton, 1981), investigating a granodiorite, found no dynamic strength increase at strain rates up to 2 s^{-1}. (Kumar, 1968) found that dynamic strength increase of granite occurred at loading rates greater than ~700 GPa s^{-1} which, for the elastic modulus of the Malsburg granite, corresponds to a strain rate of ~20 s^{-1}. Similarly, (Li et al., 2005) found a slight strength increase in a granite from strain rates between 20 and 60 s^{-1}. Furthermore, (Xia et al., 2008) found an increase in strength with strain rate in granite from rates between 60 and 160 s^{-1}. More recently, (Li et al.,

2018) determined the characteristic strain rate of a granite to be 135 s^{-1}. However, they treated the exponent of the scaling relationship as a free parameter, using a value of 0.83. While not explicitly describing the critical rate for dynamic strengthening, (Yuan et al., 2011) found that a critical strain rate of ~250 s^{-1} was required to cause pulverization of the Westerly Granite. Larger characteristic strain rates have been suggested, such as ~1000s^{-1} for a tonalite (Perkins et al., 1970), depending on initial temperature. (Doan and Gary, 2009), investigating an unusually weak granite from the damage zone of the San Andreas fault (σ_0 = ~60 MPa), observed fragmentation of their samples beyond strain rates of 100-150 s^{-1}, and found an undamaged granite underwent fragmentation at rates > ~250 s^{-1}. Here, we have precisely quantified the characteristic strain rate for dynamic behavior in typical felsic crystalline rocks. The values for the three experimental suites are within uncertainty of each other, with an average value (and pooled standard deviation) of 229 ± 81 s^{-1}, indicating that dynamic strength becomes significant above a transition strain rate of ~22.9 s^{-1}, this result is consistent with the majority of previous studies.

Compared to the data compilation in (Johnson and DeGraff, 1988), our measured values of the quasi-static elastic modulus and Poisson's ratio in the Malsburg Granite and Maggia Gneiss are consistent with typical values for granite (26.2 GPa < E < 75.5 GPa, 0.10 < ν < 0.39) and gneiss (16.8 GPa < E < 81.0 GPa, 0.08 < ν < 0.40) respectively. Our results suggest that the elastic modulus of rocks under dynamic loading is generally less than or equal to the quasi-static elastic modulus, although all SHPB experiments have considerable scatter. This is inconsistent with the generally held view, based on experiments on geological materials (Kumar, 1968; Perkins et al., 1970) and concrete (Bischoff and Perry, 1991), that elastic modulus should increase with strain rate (see (Zhang and Zhao, 2014)). Nevertheless, we note that some SHPB experiments on rock materials show no change in elastic modulus with strain rate (Frew et al., 2001; Li et al., 2005), while small decreases of elastic modulus have been observed at intermediate strain rates (Zhao et al., 1999). Indeed, (Goldsmith et al., 1976) demonstrated that elastic modulus can increase, decrease, and remain constant with increasing rate for three orthogonal directions within an anisotropic granite. The behavior of elastic properties with varying strain rate thus appears not to follow a simple trend for geological materials, instead perhaps varying dependent on the micro-structural properties of the specific lithology. This seems to be supported by the results of (Zwiessler et al., 2017), which show a

dynamic increase in the elastic modulus of a marble while at the same conditions, no dynamic change can be seen in a sandstone.

Limited work has been carried out to investigate the effect of anisotropy in dynamic loading. (Howe et al., 1974), in experiments on marble with anisotropy due to the bedding foliation of the protolith, demonstrated that dynamic strength increase is greater when compression is perpendicular to the plane of isotropy, i.e. that compression perpendicular to the foliation has a smaller characteristic strain rate. (Goldsmith et al., 1976) investigated the mechanically anisotropic Barre Granite, and found a lack of simple relationship between anisotropy, strength, and elastic moduli, although they did find that dynamic strengthening was more effective in the direction of highest elastic modulus. However, more recently, (Xia et al., 2008) attempted to repeat the experiments of (Goldsmith et al., 1976) and found no consistent strength anisotropy and no difference in dynamic strengthening with orientation. This study demonstrates that, within uncertainties, characteristic strain rate is not strongly controlled by anisotropy.

4.1 Characteristic Strain Rate and Fragment Sizes

In this study, we have determined the characteristic stress and strain rate, σ_0 and $\dot{\varepsilon}_0$ respectively, of materials by fitting experimental data to the universal scaling relationship of (Kimberley et al., 2013) (**Equation 1**). The relationship is derived from scaling of the results of a model of brittle failure in compression (Paliwal and Ramesh, 2008), where the failure process is controlled by the loading rate combined with the interaction of the initial defect distribution, the growth of wing cracks, and the interaction of those cracks. The scaling quantities, σ_0 and $\dot{\varepsilon}_0$, are formulated by combining microstructurally relevant time and length scales, and are a function of three material properties; Mode I fracture toughness, K_{IC}, elastic modulus, E, and p-wave velocity, v_p, as well as two microstructural properties; flaw density, η, and flaw size, $\bar{s}$:

$$\sigma_0 = \alpha \frac{K_{IC}}{\bar{s}\eta^{1/4}}, \textbf{(6)}$$

$$\dot{\varepsilon}_0 = \alpha \frac{v_p}{\bar{s}} \frac{K_{IC}}{E} \eta^{1/4}, \textbf{(7)}$$

where the constant $\alpha \approx 2.4$. The material and micro-structural properties are variably difficult to quantify, in particular, flaw density and size are extremely challenging to measure in a material (Housen and Holsapple, 1999). One potential problem with the scaling relationship is that there is an assumption that fracture toughness is a constant, even though a number of studies demonstrate that fracture toughness depends on loading rate and varies between initiation and propagation (Bhat et al., 2012; Chen et al., 2009; Dai and Xia, 2013; Gao et al., 2015; Xu et al., 2016). Nevertheless, from these equations it can be seen that characteristic strain rate is not independent of the characteristic stress, and can be expressed as:

$$\dot{\varepsilon}_0 = \sigma_0 \frac{v_p}{E} \eta^{1/2}. \textbf{ (8)}$$

It is therefore curious that the Maggia Gneiss in different orientations produces the same critical strain rate, despite having different measured uniaxial compressive strengths, p-wave velocities, and elastic moduli. To compensate for the variability, the flaw density, η, would need to be an anisotropic property, varying depending on orientation. "Flaw density", therefore, represents the available flaw density for the applied stress. From rearranging **Equation 8**, the available flaw densities for the applied stress of the Maggia Gneiss (parallel) and Maggia Gneiss (perpendicular) are 233.3 m^{-2} and 120.3 m^{-2} respectively.

The variability of the available flaw density by orientation is likely to be controlled by the rock fabric, in particular the arrangement of biotite grains controlling the orientation in which fractures can propagate (**Figure 6**). Biotite is a tabular mineral that develops a prominent cleavage in the basal plane (i.e. parallel to the large plate-like faces of the mineral). Mode I fractures form parallel to the direction of maximum principal compression, thus fracturing is more readily facilitated when the basal planes of the biotite grains are aligned with the maximum principal stress, as in the case of the Maggia Gneiss (parallel). This is consistent with observations of the resultant sample from the quasi-static and low rate SHPB experiments; Maggia Gneiss (parallel) foliation planes are commonly used as fracture planes, and the samples fragment into plate-like pieces (**Figure 6e**). In contrast, the Maggia Gneiss (perpendicular) fails with dominant fractures at an inclined angle to the compression axis. The resultant fragments are more equant and polyhedral (**Figure 6f**). Differences between failure modes could not be distinguished for the heavily fragmented samples due to the extensive nature of the fragmentation. The behavior and activation of Mode I fractures in relation to the pre-existing available flaw distribution therefore seems to play a role in the fragmentation of

rocks. In turn, this may be responsible for the variation of the power law exponent, N, of fragment sizes as a function of strain rate between the two orientations of Maggia Gneiss. Curiously, the value of N for the Malsburg Granite is similar to, though slightly less than that of the Maggia Gneiss (parallel). The Malsburg granite also contains biotite, however, unlike the Maggia Gneiss there is no alignment of those biotite grains. However, we find that the calculated flaw density of the Marlsburg Granite is 228.0 m^{-2} (**Equation 8**), similar though slightly less than the flaw density of the Maggia Gneiss (parallel). Thus, the available flaw density is correlated with N. Larger flaw densities correspond to larger values of N, i.e. large available flaw densities result in smaller fragments at low rates, but larger average fragment sizes at very high rates.

4.2 Comparison with Fragmentation Models

Each material in this study follows a power-law relationship between fragment size and strain rate. All current fragmentation models (Glenn and Chudnovsky, 1986; Grady, 2007; Levy and Molinari, 2010; Zhou et al., 2006b, 2006a), which model tensile failure, predict that the exponent of the power-law relationship between fragment size and strain rate at high strain rates is $-{}^{2}/_{3}$; at low strain rates, all but the Grady model predict that fragment size approaches a constant value. Here, the exponent of each compressive fragmentation relationship, N, is significantly different from the predicted exponent for tensile failure (**Table 1**). Furthermore, despite the characteristic strain rate for each experiment suite being the same within error, there is a statistically significant difference between the exponents of the power-law relationships. (Ghaffari et al., 2019) also noted dissimilarity between their measured exponent, N, from SHPB experiments and the expected exponent. However, their measured exponent, N, of -0.42 is greater than the expected exponent, unlike our results.

Failure in tension is entirely different to failure in compression (Jaeger et al., 2009), consequently tensile fragmentation models cannot be directly compared to compressive experiments. Compressive loading can make a material quite different to its pristine condition by creating, activating, and growing internal defects (Hogan et al., 2016), and, brittle materials in compression can store large amounts of strain energy which, when released, can generate very fine fragments (Ramesh et al., 2015). A method to convert compressive strain rate to an equivalent tensile strain rate has been made by (Hogan et al., 2016; Ramesh et al., 2015). Here, we follow and adapt that reasoning (See **Supplementary Text 2** for details). The results of calculating the equivalent tensile strain rate and scaling the rate and fragment sizes are shown in **Figure 7**. Importantly, the scaling causes all of the experimental suites to collapse onto a

single power law with an exponent of -2.63 ± 0.23. This occurs because the scaling of fragment size accounts for the anisotropy of the material; fracture toughness being an anisotropic property. Nevertheless, the exponent of the power law remains very different to the exponents predicted by tensile fragmentation models, which consistently predict an exponent of $-{}^{2}/_{3}$. The expected exponent of the fragmentation models is a consequence of the assumption of complete conversion of the kinetic energy released in fragmentation ($U_k \propto s^5\dot{\varepsilon}^2$) to fracture surface energy ($U_s \propto s^2$) (Grady, 1982). Our results suggest that this energy balance argument is missing at least one term, or that assuming equilibrium or near-equilibrium fragmentation in compressive dynamic failure of rocks is incorrect (Grady, 2010). Additionally, our results are at similar scaled equivalent tensile strain rates to the transition between the quasi-static and dynamic regimes predicted in the fragmentation models of (Glenn and Chudnovsky, 1986; Levy and Molinari, 2010; Zhou et al., 2006a, 2006b), however, our results show no indication of a flattening of the fragment size to a constant value at low strain rates.

An additional consideration of this comparison between average fragment size from these experiments with tensile fragmentation models is that we have obtained the median fragment size from mass-size distributions. The fragment size estimated from the tensile fragmentation models are the average fragment sizes from a number-size distribution. Mass-size distributions cannot be converted, without introducing large uncertainty, to number-size distributions. Average sizes from mass-size distributions are always larger than the average from number-size distributions. Furthermore, the average grain sizes are more strongly affected by this effect where there are larger numbers of grains, i.e. the samples that experienced higher strain rates and fragmented more. This suggests that the value of the exponent, N, if we could have measured the average from number-size distributions, would be even more negative and different from the expected value of $-{}^{2}/_{3}$.

4.3 Implications for Impact Cratering and Geohazards

Brittle deformation under quasi-static conditions is only weakly sensitive to the loading rate, but responds to confinement, pore fluid pressure, and damage (Holsapple, 2009). This study shows that felsic crystalline rocks under uniaxial compression experience significant rate dependent effects beyond transition strain rates of ~22.9 s^{-1}. Beyond this rate, strength increases considerably (**Figure 2**) and the resultant products of that deformation are characterized by progressively smaller fragments (**Figure 5**). Here, we discuss where the application of these

results is relevant in terms of the understanding of impact cratering and other fast geological processes.

During hypervelocity impact events, deformation occurs at large strain rates. This deformation can occur during shock loading, but also during subsequent excavation of the transient cavity and potentially along shear zones during crater collapse. The most extreme instantaneous conditions experienced during hypervelocity impact are a result of shock loading. The highest compressive strain rate in an impact, related to the rise time of the shock wave, can be approximated by the inverse of the time required for projectile to couple with the target, $\dot{\varepsilon}_{max} = v_i/a$, where v_i and a are the projectile velocity and diameter respectively (Melosh et al., 1992). We note that this value may also be affected by solid-state viscosity and the shock amplitude (Swegle and Grady, 1985). Consequently, for a typical impact velocity on Earth of 20.5 km s^{-1} (Le Feuvre and Wieczorek, 2011), strain rates in excess of 22.9 s^{-1} will be experienced for any impact with any projectile smaller than ~1 km in diameter. In reality, rate-dependent effects as observed in this study may not be applicable for impact events with projectile diameters as large as 1 km. Stress conditions during shock are very different to the uniaxial conditions studied here. Rock strength at large pressures is primarily controlled by ductile plastic flow rather than brittle failure (Holsapple, 2009). Under these conditions, as experienced during shock, rock strength is similar for rocks during quasi-static and dynamic loading, indicating that rate-dependent strength increase has a negligible effect at confining pressures greater than the pressure threshold for ductile plastic flow (Kimberley et al., 2013). This is supported by experimental observations that increased confining pressures lead to less effective fragmentation (Yuan et al., 2011). It is only after shock compression, during crater excavation and modification, where confining stresses are comparable to the experiments in this study. In the later stages of impact cratering, strain rates may be several orders of magnitude less than the strain rate experienced during shock (Kenkmann et al., 2014).

To demonstrate where and when strain rates are high enough and confining stresses are low enough during impact cratering for dynamic strength and fragmentation to play an important role, we ran several simulations of impacts into a granitic target with the iSALE shock physics code (See **Supplementary Text 3**). The simulations demonstrate that a large volume of rocks experience strain rates greater than 22.9 s^{-1} simultaneously to confining pressures up to a nominal upper value of 500 MPa for all impacts with an impactor diameter up to ~100m (**Figure 8; Supplementary Videos 1-4**).

The effective strength of rock masses is known to decrease with increasing scale (e.g. (Hoek et al., 2002)), and is often adjusted for in impact cratering simulations. Thus, the characteristic strain rate may also vary with increasing scale. The characteristic strain rate for dynamic tensile fragmentation in impacts has been predicted to scale inversely with target volume (Melosh et al., 1992), although it is unclear whether the transition rate for compressive fragmentation scales in the same way, it is possible that this scaling may compensate for at least some of the decrease in strain rate associated with increasing impact size, leading to increased dynamic deformation in impacts with larger impactor diameters than 100 m. Additionally, iSALE does not accurately describe the deformation of individual faults; where deformation is localized onto faults strain rates may also exceed the transition strain rate for dynamic behavior.

Although rate-dependent effects are most important on the small scale, experiments at those scales provide ground-truth for all numerical models. Large scale impact events may have rates sufficiently low that rate effects become negligible, however to be accurate, models must still include those rate effects (Holsapple, 2009). Without them, models are unable to use direct laboratory-measured rock strength properties to accurately model laboratory-scale impact experiments, which is one of the simplest ways to test and ground-truth those models. Generally, numerical impact models do not incorporate rate-dependency in their constitutive models. To get around the issue, numerical models of laboratory scale impact experiments typically make simplistic adjustments to strength properties in order to produce craters of the correct size (e.g. (Winkler et al., 2018)). One exception to this is the Grady-Kipp fragmentation model which incorporates rate dependency as a consequence of an initial flaw distribution and the time-dependent growth of fractures (Grady and Kipp, 1985, 1980; Melosh et al., 1992; Wiggins et al., 2019). Unfortunately, the Grady-Kipp model was developed only for tensile failure. It is currently unclear how the Grady-Kipp model could be extended to compressive failure (Melosh, 2017). The results of this work provide a potential ground-truth for implementations of dynamic compressive strength and fragmentation in numerical impact simulation.

In addition to impact cratering, rate-dependent brittle compressive failure could have significant effects in endogenic geological processes such as earthquake rupture and landslides. Strain rates in the vicinity of a fracture tip in a sub-sonic seismogenic rupture can be up to 10^5 s^{-1}, but decay rapidly with distance from the fault zone (Reches and Dewers, 2005). During super-shear rupture, strain rates are likely to be even higher, and to be distributed over a wider area (Doan and Gary, 2009). Extensive rock pulverization can be found in the vicinity of a number of large faults; San Andreas (Dor et al., 2006a, 2006b; Rempe et al., 2013; Rockwell

et al., 2009; Wechsler et al., 2011; Wilson et al., 2005), San Jacinto (Dor et al., 2006b; Wechsler et al., 2009), North Anatolia (Dor et al., 2008), Arima-Takatsuki (Mitchell et al., 2011), Garlock (Rockwell et al., 2009), and Foiana (Fondriest et al., 2015). Pulverization around these fault zones may therefore be a result of fragmentation during dynamic compressive rock failure. However, in the absence of super-shear rupture, it is challenging to explain how compressive strain rates could be large enough to produce pulverized fault rocks up to 100 m away a fault core (Aben et al., 2017). Experiments and numerical simulations suggest that dynamic tension, rather than compression, may be responsible (Xu and Ben-Zion, 2017; Griffith et al. 2018). Nevertheless, the results of this study provide experimental comparison to assess the potential role of dynamic compressive rock failure in seismogenic rupture, including the mapping of dynamic conditions away from fault zones. Rock pulverization is also observed in landslides, where breccia deposits are composed of finely crushed rock with prevalence of matrix material (Crosta et al., 2007; Dunning and Armitage, 2011). Dynamic fragmentation has even been suggested to be responsible for the motion of long-runout landslides (Davies and McSaveney, 2009; McSaveney and Davies, 2006). However, limited comparisons have been made between the products of landslides and experiments.

5 Conclusions

Here, we have demonstrated that felsic crystalline rocks have characteristic strain rates for rate-dependency that are within uncertainty of each other with an average value of 229 ± 81 s^{-1}, i.e. those rocks experience significant dynamic strength effects above transition strain rates of ~22.9 s^{-1}. These rates are independent of any anisotropy in those rocks, regardless of strength differences. The average fragment sizes of rocks that fail in the dynamic compression regime are described by a power law function of strain rate. The exponent of that power law is inconsistent with current fragmentation models but may be related to the distribution and orientation of flaws in geomaterials. The results of this study may have important applications to impact processes and other catastrophic geohazards.

Acknowledgments and Data Availability

The authors wish to acknowledge Herbert Ickler and Gordon Mette for preparation of samples. Louis Müller and Matthias Dörfler are thanked for their assistance in conducting experiments. Additionally, Sebastian Hess of the Ernst-Mach Institute is thanked for technical assistance with the SHPB. We gratefully acknowledge the developers of iSALE-2D, including

Gareth Collins, Kai Wünnemann, Dirk Elbeshausen, Tom Davison, Boris Ivanov and Jay Melosh. Some plots in this work were created with the pySALEPlot tool written by Tom Davison. We would like to thank two anonymous reviewers for their work and their constructive comments. All data presented within this publication can be found at http://www.doi.org/10.5281/zenodo.3987223. This work was funded by DFG Project KE 732/27-1.

References

Aben, F.M., Doan, M.-L., Gratier, J.-P., Renard, F., 2017. Coseismic Damage Generation and Pulverization in Fault Zones, in: Fault Zone Dynamic Processes. American Geophysical Union (AGU), pp. 47–80. https://doi.org/10.1002/9781119156895.ch4

Aben, F.M., Doan, M.-L., Mitchell, T.M., Toussaint, R., Reuschlé, T., Fondriest, M., Gratier, J.-P., Renard, F., 2016. Dynamic fracturing by successive coseismic loadings leads to pulverization in active fault zones. Journal of Geophysical Research: Solid Earth 121, 2338–2360. https://doi.org/10.1002/2015JB012542

Agarwal, A., Poelchau, M.H., Kenkmann, T., Rae, A., Ebert, M., 2019. Impact Experiment on Gneiss: The Effects of Foliation on Cratering Process. Journal of Geophysical Research: Solid Earth 124, 13532–13546. https://doi.org/10.1029/2019JB018345

Barber, T., Griffith, W.A., 2017. Experimental constraints on dynamic fragmentation as a dissipative process during seismic slip. Philosophical Transactions of the Royal Society A: Mathematical, Physical and Engineering Sciences 375, 20160002. https://doi.org/10.1098/rsta.2016.0002

Bhat, H.S., Rosakis, A.J., Sammis, C.G., 2012. A Micromechanics Based Constitutive Model for Brittle Failure at High Strain Rates. J. Appl. Mech 79. https://doi.org/10.1115/1.4005897

Bischoff, P.H., Perry, S.H., 1991. Compressive behaviour of concrete at high strain rates. Materials and Structures 24, 425–450. https://doi.org/10.1007/BF02472016

Blanton, T.L., 1981. Effect of strain rates from 10-2 to 10 sec-1 in triaxial compression tests on three rocks. International Journal of Rock Mechanics and Mining Sciences & Geomechanics Abstracts 18, 47–62. https://doi.org/10.1016/0148-9062(81)90265-5

Chen, R., Xia, K., Dai, F., Lu, F., Luo, S.N., 2009. Determination of dynamic fracture parameters using a semi-circular bend technique in split Hopkinson pressure bar testing. Engineering Fracture Mechanics 76, 1268–1276. https://doi.org/10.1016/j.engfracmech.2009.02.001

Chen, W.W., Song, B., 2010. Split Hopkinson (Kolsky) Bar: Design, Testing and Applications. Springer Science & Business Media.

Crosta, G.B., Frattini, P., Fusi, N., 2007. Fragmentation in the Val Pola rock avalanche, Italian Alps. Journal of Geophysical Research: Earth Surface 112. https://doi.org/10.1029/2005JF000455

Dai, F., Xia, K.W., 2013. Laboratory measurements of the rate dependence of the fracture toughness anisotropy of Barre granite. International Journal of Rock Mechanics and Mining Sciences 60, 57–65. https://doi.org/10.1016/j.ijrmms.2012.12.035

Davies, T.R., McSaveney, M.J., 2009. The role of rock fragmentation in the motion of large landslides. Engineering Geology, The Mechanics and Velocity of Large Landslides 109, 67–79. https://doi.org/10.1016/j.enggeo.2008.11.004

Doan, M.-L., Gary, G., 2009. Rock pulverization at high strain rate near the San Andreas fault. Nature Geoscience 2, 709–712. https://doi.org/10.1038/ngeo640

Dor, O., Ben-Zion, Y., Rockwell, T.K., Brune, J., 2006a. Pulverized rocks in the Mojave section of the San Andreas Fault Zone. Earth and Planetary Science Letters 245, 642–654. https://doi.org/10.1016/j.epsl.2006.03.034

Dor, O., Rockwell, T.K., Ben-Zion, Y., 2006b. Geological Observations of Damage Asymmetry in the Structure of the San Jacinto, San Andreas and Punchbowl Faults in Southern California: A Possible Indicator for Preferred Rupture Propagation Direction. Pure appl. geophys. 163, 301–349. https://doi.org/10.1007/s00024-005-0023-9

Dor, O., Yildirim, C., Rockwell, T.K., Ben-Zion, Y., Emre, O., Sisk, M., Duman, T.Y., 2008. Geological and geomorphologic asymmetry across the rupture zones of the 1943 and 1944 earthquakes on the North Anatolian Fault: Possible signals for preferred earthquake propagation direction. Geophys J Int 173, 483–504. https://doi.org/10.1111/j.1365-246X.2008.03709.x

Dunning, S.A., Armitage, P.J., 2011. The Grain-Size Distribution of Rock-Avalanche Deposits: Implications for Natural Dam Stability, in: Evans, S.G., Hermanns, R.L., Strom, A., Scarascia-Mugnozza, G. (Eds.), Natural and Artificial Rockslide Dams, Lecture Notes in Earth Sciences. Springer, Berlin, Heidelberg, pp. 479–498. https://doi.org/10.1007/978-3-642-04764-0_19

Fondriest, M., Aretusini, S., Di Toro, G., Smith, S.A.F., 2015. Fracturing and rock pulverization along an exhumed seismogenic fault zone in dolostones: The Foiana Fault Zone (Southern Alps, Italy). Tectonophysics 654, 56–74. https://doi.org/10.1016/j.tecto.2015.04.015

Frew, D.J., Forrestal, M.J., Chen, W., 2001. A split Hopkinson pressure bar technique to determine compressive stress-strain data for rock materials. Experimental Mechanics 41, 40–46. https://doi.org/10.1007/BF02323102

Gao, G., Huang, S., Xia, K., Li, Z., 2015. Application of Digital Image Correlation (DIC) in Dynamic Notched Semi-Circular Bend (NSCB) Tests. Exp Mech 55, 95–104. https://doi.org/10.1007/s11340-014-9863-5

Ghaffari, H.O., Griffith, W.A., Barber, T.J., 2019. Energy delocalization during dynamic rock fragmentation. Geophys J Int 217, 1034–1046. https://doi.org/10.1093/gji/ggz064

Glenn, L.A., Chudnovsky, A., 1986. Strain-energy effects on dynamic fragmentation. Journal of Applied Physics 59, 1379–1380. https://doi.org/10.1063/1.336532

Goldsmith, W., Sackman, J.L., Ewerts, C., 1976. Static and dynamic fracture strength of Barre granite. International Journal of Rock Mechanics and Mining Sciences & Geomechanics Abstracts 13, 303–309. https://doi.org/10.1016/0148-9062(76)91829-5

Grady, D., 2009. Dynamic Fragmentation of Solids, in: Shock Wave Science and Technology Reference Library, Vol. 3: Solids II. Springer, Berlin, Heidelberg, pp. 169–276. https://doi.org/10.1007/978-3-540-77080-0_4

Grady, D., 2007. Fragmentation of Rings and Shells: The Legacy of N.F. Mott. Springer Science & Business Media.

Grady, D.E., 2010. Length scales and size distributions in dynamic fragmentation. Int J Fract 163, 85–99. https://doi.org/10.1007/s10704-009-9418-4

Grady, D.E., 1982. Local inertial effects in dynamic fragmentation. Journal of Applied Physics 53, 322–325. https://doi.org/10.1063/1.329934

Grady, D.E., Kipp, M.E., 1985. Mechanisms of dynamic fragmentation: Factors governing fragment size. Mechanics of Materials 4, 311–320. https://doi.org/10.1016/0167-6636(85)90028-6

Grady, D.E., Kipp, M.E., 1980. Continuum modelling of explosive fracture in oil shale. International Journal of Rock Mechanics and Mining Sciences & Geomechanics Abstracts 17, 147–157. https://doi.org/10.1016/0148-9062(80)91361-3

Green, S.J., Leasia, J.D., Perkins, R.D., Jones, A.H., 1972. Triaxial stress behavior of Solenhofen limestone and westerly granite at high strain rates. Journal of Geophysical Research (1896-1977) 77, 3711–3724. https://doi.org/10.1029/JB077i020p03711

Hahn-Weinheimer, P., Ackermann, H., 1967. Geochemical investigation of differentiated granite plutons of the Southern Black Forest—II. The zoning of the Malsburg Granite pluton as indicated by the elements titanium, zirconium, phosphorus, strontium, barium, rubidium, potassium and sodium. Geochimica et Cosmochimica Acta 31, 2197–2218. https://doi.org/10.1016/0016-7037(67)90061-0

Hoek, E., Carranza-Torres, C., Corkum, B., 2002. Hoek-Brown failure criterion-2002 edition. Proceedings of NARMS-Tac 1, 267–273.

Hogan, J.D., Castillo, J.A., Rawle, A., Spray, J.G., Rogers, R.J., 2013. Automated microscopy and particle size analysis of dynamic fragmentation in natural ceramics. Engineering Fracture Mechanics 98, 80–91. https://doi.org/10.1016/j.engfracmech.2012.11.021

Hogan, J.D., Farbaniec, L., Daphalapurkar, N., Ramesh, K.T., 2016. On Compressive Brittle Fragmentation. Journal of the American Ceramic Society 99, 2159–2169. https://doi.org/10.1111/jace.14171

Hogan, J.D., Rogers, R.J., Spray, J.G., Boonsue, S., 2012. Dynamic fragmentation of granite for impact energies of 6–28J. Engineering Fracture Mechanics 79, 103–125. https://doi.org/10.1016/j.engfracmech.2011.10.006

Holsapple, K.A., 2009. On the "strength" of the small bodies of the solar system: A review of strength theories and their implementation for analyses of impact disruptions. Planetary and Space Science, Catastrophic Disruption in the Solar System 57, 127–141. https://doi.org/10.1016/j.pss.2008.05.015

Housen, K.R., Holsapple, K.A., 1999. Scale Effects in Strength-Dominated Collisions of Rocky Asteroids. Icarus 142, 21–33. https://doi.org/10.1006/icar.1999.6206

Howe, S.P., Goldsmith, W., Sackman, J.L., 1974. Macroscopic static and dynamic mechanical properties of Yule marble. Experimental Mechanics 14, 337–346. https://doi.org/10.1007/BF02323559

Jaeger, J.C., Cook, N.G.W., Zimmerman, R., 2009. Fundamentals of Rock Mechanics. John Wiley & Sons.

Johnson, R.B., DeGraff, J.V., 1988. Principles of Engineering Geology. Wiley.

Kenkmann, T., Poelchau, M.H., Wulf, G., 2014. Structural geology of impact craters. Journal of Structural Geology 62, 156–182. https://doi.org/10.1016/j.jsg.2014.01.015
Kimberley, J., Ramesh, K.T., Daphalapurkar, N.P., 2013. A scaling law for the dynamic strength of brittle solids. Acta Materialia 61, 3509–3521. https://doi.org/10.1016/j.actamat.2013.02.045
Kumar, A., 1968. The effect of stress rate and temperature on the strength of basalt and granite. GEOPHYSICS 33, 501–510. https://doi.org/10.1190/1.1439947
Lankford, J., Blanchard, C.R., 1991. Fragmentation of brittle materials at high rates of loading. J Mater Sci 26, 3067–3072. https://doi.org/10.1007/BF01124844
Le Feuvre, M., Wieczorek, M.A., 2011. Nonuniform cratering of the Moon and a revised crater chronology of the inner Solar System. Icarus 214, 1–20. https://doi.org/10.1016/j.icarus.2011.03.010
Levy, S., Molinari, J.F., 2010. Dynamic fragmentation of ceramics, signature of defects and scaling of fragment sizes. Journal of the Mechanics and Physics of Solids 58, 12–26. https://doi.org/10.1016/j.jmps.2009.09.002
Li, X.B., Lok, T.S., Zhao, J., 2005. Dynamic Characteristics of Granite Subjected to Intermediate Loading Rate. Rock Mech. Rock Engng. 38, 21–39. https://doi.org/10.1007/s00603-004-0030-7
Li, X.F., Li, H.B., Zhang, Q.B., Jiang, J.L., Zhao, J., 2018. Dynamic fragmentation of rock material: Characteristic size, fragment distribution and pulverization law. Engineering Fracture Mechanics 199, 739–759. https://doi.org/10.1016/j.engfracmech.2018.06.024
McSaveney, M.J., Davies, T.R.H., 2006. Rapid rock mass flow with dynamic fragmentation: Inferences from the morphology and internal structure of rockslides and rock avalanches, in: Evans, S.G., Mugnozza, G.S., Strom, A., Hermanns, R.L. (Eds.), Landslides from Massive Rock Slope Failure, NATO Science Series. Springer Netherlands, Dordrecht, pp. 285–304. https://doi.org/10.1007/978-1-4020-4037-5_16
Melosh, H.J., 2017. Impact Spall and Fragmentation by Near-Surface Stress Wave Interactions, in: LPSC XLVIII. p. 2051.
Melosh, H.J., Ryan, E.V., Asphaug, E., 1992. Dynamic fragmentation in impacts: Hydrocode simulation of laboratory impacts. Journal of Geophysical Research: Planets 97, 14735–14759. https://doi.org/10.1029/92JE01632
Mitchell, T.M., Ben-Zion, Y., Shimamoto, T., 2011. Pulverized fault rocks and damage asymmetry along the Arima-Takatsuki Tectonic Line, Japan. Earth and Planetary Science Letters 308, 284–297. https://doi.org/10.1016/j.epsl.2011.04.023
Mott, N.F., 1947. Fragmentation of shell cases. Proceedings of the Royal Society of London. Series A. Mathematical and Physical Sciences 189, 300–308. https://doi.org/10.1098/rspa.1947.0042
Mott, N.F., 1943. A Theory of the Fragmentation of Shells and Bombs. United Kingdom Ministry of Supply AC4035.
Paliwal, B., Ramesh, K.T., 2008. An interacting micro-crack damage model for failure of brittle materials under compression. Journal of the Mechanics and Physics of Solids 56, 896–923. https://doi.org/10.1016/j.jmps.2007.06.012
Perkins, R.D., Green, S.J., Friedman, M., 1970. Uniaxial stress behavior of porphyritic tonalite at strain rates to 103/second. International Journal of Rock Mechanics and Mining Sciences & Geomechanics Abstracts 7, 527–535. https://doi.org/10.1016/0148-9062(70)90005-7
Rae, A.S.P., Kenkmann, T., Padmanabha, V., Poelchau, M.H., Schäfer, F., 2020. Dynamic Compressive Strength and Fragmentation in Crystalline Rocks [Data set]. Zenodo. http://www.doi.org/10.5281/zenodo.3987223.
Ramesh, K.T., Hogan, J.D., Kimberley, J., Stickle, A., 2015. A review of mechanisms and models for dynamic failure, strength, and fragmentation. Planetary and Space Science, VIII Workshop on Catastrophic Disruption in the Solar System 107, 10–23. https://doi.org/10.1016/j.pss.2014.11.010
Reches, Z., Dewers, T.A., 2005. Gouge formation by dynamic pulverization during earthquake rupture. Earth and Planetary Science Letters 235, 361–374. https://doi.org/10.1016/j.epsl.2005.04.009
Rempe, M., Mitchell, T., Renner, J., Nippress, S., Ben-Zion, Y., Rockwell, T., 2013. Damage and seismic velocity structure of pulverized rocks near the San Andreas Fault. Journal of Geophysical Research: Solid Earth 118, 2813–2831. https://doi.org/10.1002/jgrb.50184
Rockwell, T., Sisk, M., Girty, G., Dor, O., Wechsler, N., Ben-Zion, Y., 2009. Chemical and Physical Characteristics of Pulverized Tejon Lookout Granite Adjacent to the San Andreas and Garlock Faults: Implications for Earthquake Physics. Pure appl. geophys. 166, 1725–1746. https://doi.org/10.1007/s00024-009-0514-1
Swegle, J.W., Grady, D.E., 1985. Shock viscosity and the prediction of shock wave rise times. Journal of Applied Physics 58, 692–701. https://doi.org/10.1063/1.336184
Turcotte, D.L., 1986. Fractals and fragmentation. Journal of Geophysical Research: Solid Earth 91, 1921–1926. https://doi.org/10.1029/JB091iB02p01921

Wang, H., Ramesh, K.T., 2004. Dynamic strength and fragmentation of hot-pressed silicon carbide under uniaxial compression. Acta Materialia 52, 355–367. https://doi.org/10.1016/j.actamat.2003.09.036
Wechsler, N., Allen, E.E., Rockwell, T.K., Girty, G., Chester, J.S., Ben-Zion, Y., 2011. Characterization of pulverized granitoids in a shallow core along the San Andreas Fault, Littlerock, CA. Geophys J Int 186, 401–417. https://doi.org/10.1111/j.1365-246X.2011.05059.x
Wechsler, N., Rockwell, T.K., Ben-Zion, Y., 2009. Application of high resolution DEM data to detect rock damage from geomorphic signals along the central San Jacinto Fault. Geomorphology, Understanding earth surface processes from remotely sensed digital terrain models 113, 82–96. https://doi.org/10.1016/j.geomorph.2009.06.007
Wiggins, S.E., Johnson, B.C., Bowling, T.J., Melosh, H.J., Silber, E.A., 2019. Impact Fragmentation and the Development of the Deep Lunar Megaregolith. Journal of Geophysical Research: Planets 124, 941–957. https://doi.org/10.1029/2018JE005757
Wilson, B., Dewers, T., Reches, Z., Brune, J., 2005. Particle size and energetics of gouge from earthquake rupture zones. Nature 434, 749–752. https://doi.org/10.1038/nature03433
Winkler, R., Luther, R., Poelchau, M.H., Wünnemann, K., Kenkmann, T., 2018. Subsurface deformation of experimental hypervelocity impacts in quartzite and marble targets. Meteoritics & Planetary Science 53, 1733–1755. https://doi.org/10.1111/maps.13080
Xia, K., Nasseri, M.H.B., Mohanty, B., Lu, F., Chen, R., Luo, S.N., 2008. Effects of microstructures on dynamic compression of Barre granite. International Journal of Rock Mechanics and Mining Sciences 45, 879–887. https://doi.org/10.1016/j.ijrmms.2007.09.013
Xia, K., Yao, W., 2015. Dynamic rock tests using split Hopkinson (Kolsky) bar system – A review. Journal of Rock Mechanics and Geotechnical Engineering 7, 27–59. https://doi.org/10.1016/j.jrmge.2014.07.008
Xu, Y., Dai, F., Xu, N.W., Zhao, T., 2016. Numerical Investigation of Dynamic Rock Fracture Toughness Determination Using a Semi-Circular Bend Specimen in Split Hopkinson Pressure Bar Testing. Rock Mech Rock Eng 49, 731–745. https://doi.org/10.1007/s00603-015-0787-x
Yao, W., Xu, Y., Xia, K., 2020. Damage Evolution During Rock Pulverization Induced by Dynamic Compressive Loading. Journal of Geophysical Research: Solid Earth 125, e2020JB019388. https://doi.org/10.1029/2020JB019388
Yuan, F., Prakash, V., Tullis, T., 2011. Origin of pulverized rocks during earthquake fault rupture. Journal of Geophysical Research: Solid Earth 116. https://doi.org/10.1029/2010JB007721
Zhang, Q.B., Zhao, J., 2014. A Review of Dynamic Experimental Techniques and Mechanical Behaviour of Rock Materials. Rock Mech Rock Eng 47, 1411–1478. https://doi.org/10.1007/s00603-013-0463-y
Zhao, J., Li, H.B., Wu, M.B., Li, T.J., 1999. Dynamic uniaxial compression tests on a granite. International Journal of Rock Mechanics and Mining Sciences 36, 273–277. https://doi.org/10.1016/S0148-9062(99)00008-X
Zhou, F., Molinari, J.-F., Ramesh, K.T., 2006a. Analysis of the brittle fragmentation of an expanding ring. Computational Materials Science, Proceedings of the 14th International Workshop on Computational Mechanics of Materials 37, 74–85. https://doi.org/10.1016/j.commatsci.2005.12.017
Zhou, F., Molinari, J.-F., Ramesh, K.T., 2006b. Effects of material properties on the fragmentation of brittle materials. Int J Fract 139, 169–196. https://doi.org/10.1007/s10704-006-7135-9
Zwiessler, R., Kenkmann, T., Poelchau, M.H., Nau, S., Hess, S., 2017. On the use of a split Hopkinson pressure bar in structural geology: High strain rate deformation of Seeberger sandstone and Carrara marble under uniaxial compression. Journal of Structural Geology 97, 225–236. https://doi.org/10.1016/j.jsg.2017.03.007

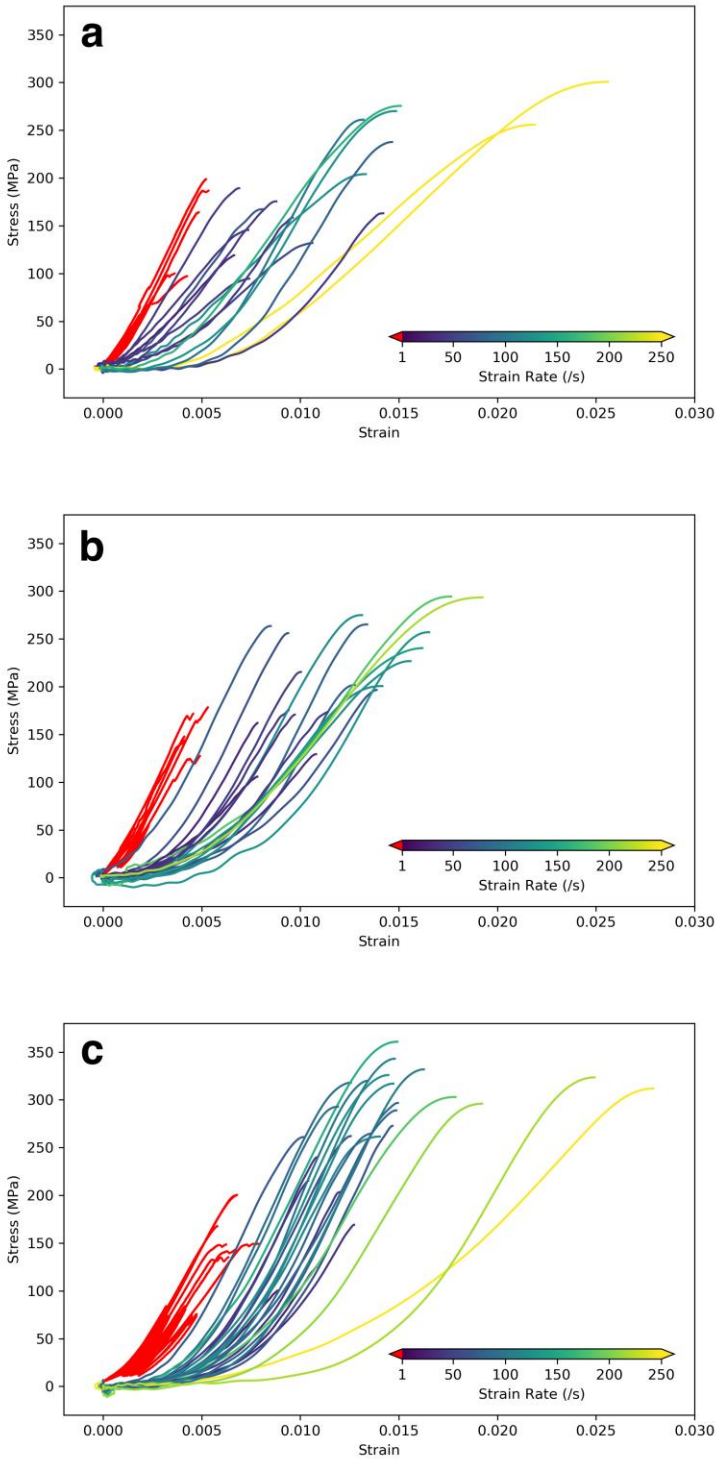

Figure 1. Stress-Strain curves for a) Malsburg Granite, b) Maggia Gneiss (parallel), and c) Maggia Gneiss (perpendicular). Quasi-static experiments are colored red, while dynamic experiments are colored by strain rate.

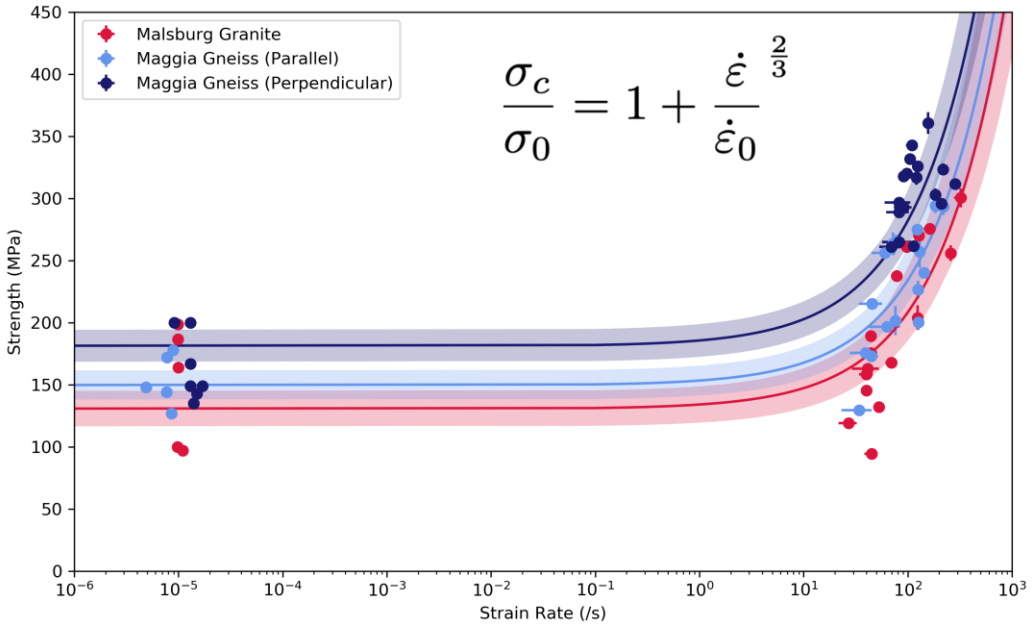

Figure 2. Compressive strengths from quasi-static and dynamic testing at various strain rates. Each suite follows the universal scaling relationship of (Kimberley et al., 2013), each fitted curve is shown with 1σ error envelopes. Data presented with a linear x-axis are shown in **Supplementary Figure 2**.

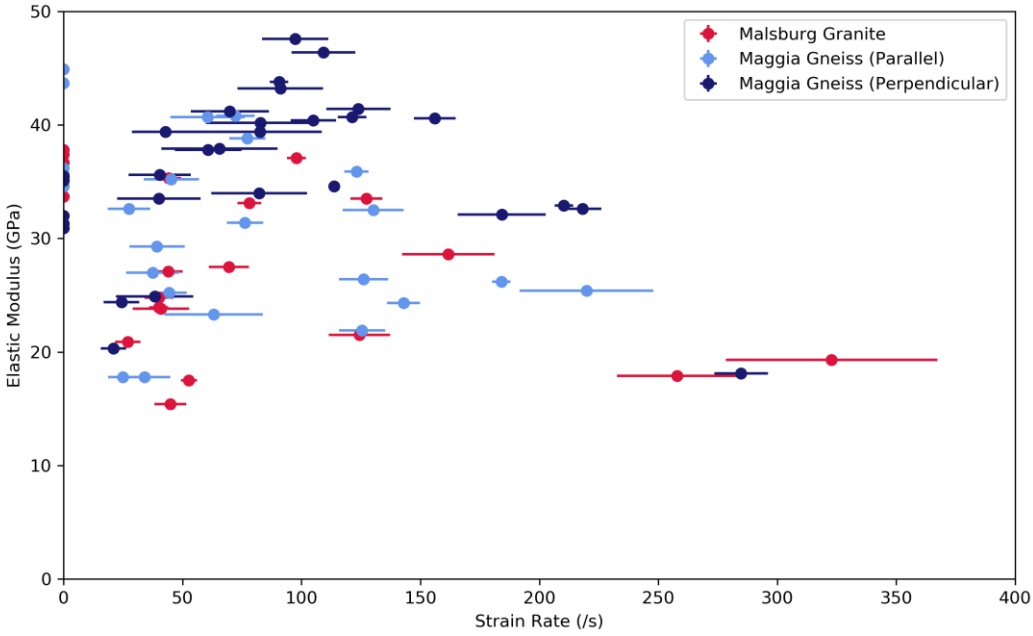

Figure 3. Elastic modulus from quasi-static and dynamic testing at various strain rates. Data presented with a logarithmic x-axis are shown in **Supplementary Figure 3**.

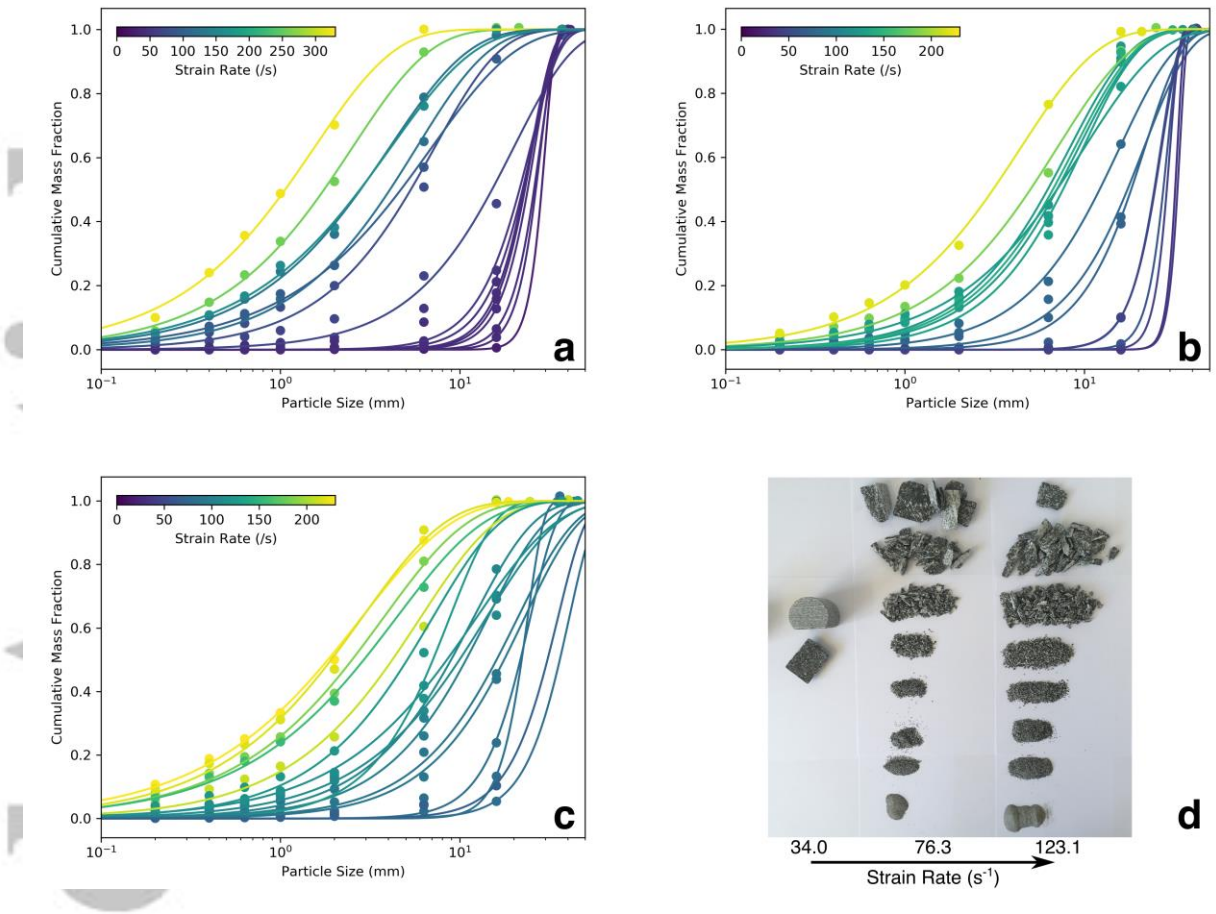

Figure 4. Cumulative mass fragment size distributions colored by strain rate for a) Malsburg Granite, b) Maggia Gneiss (parallel), and c) Maggia Gneiss (perpendicular). d) Photograph of fragments from Maggia Gneiss (parallel) experiments at various strain rates.

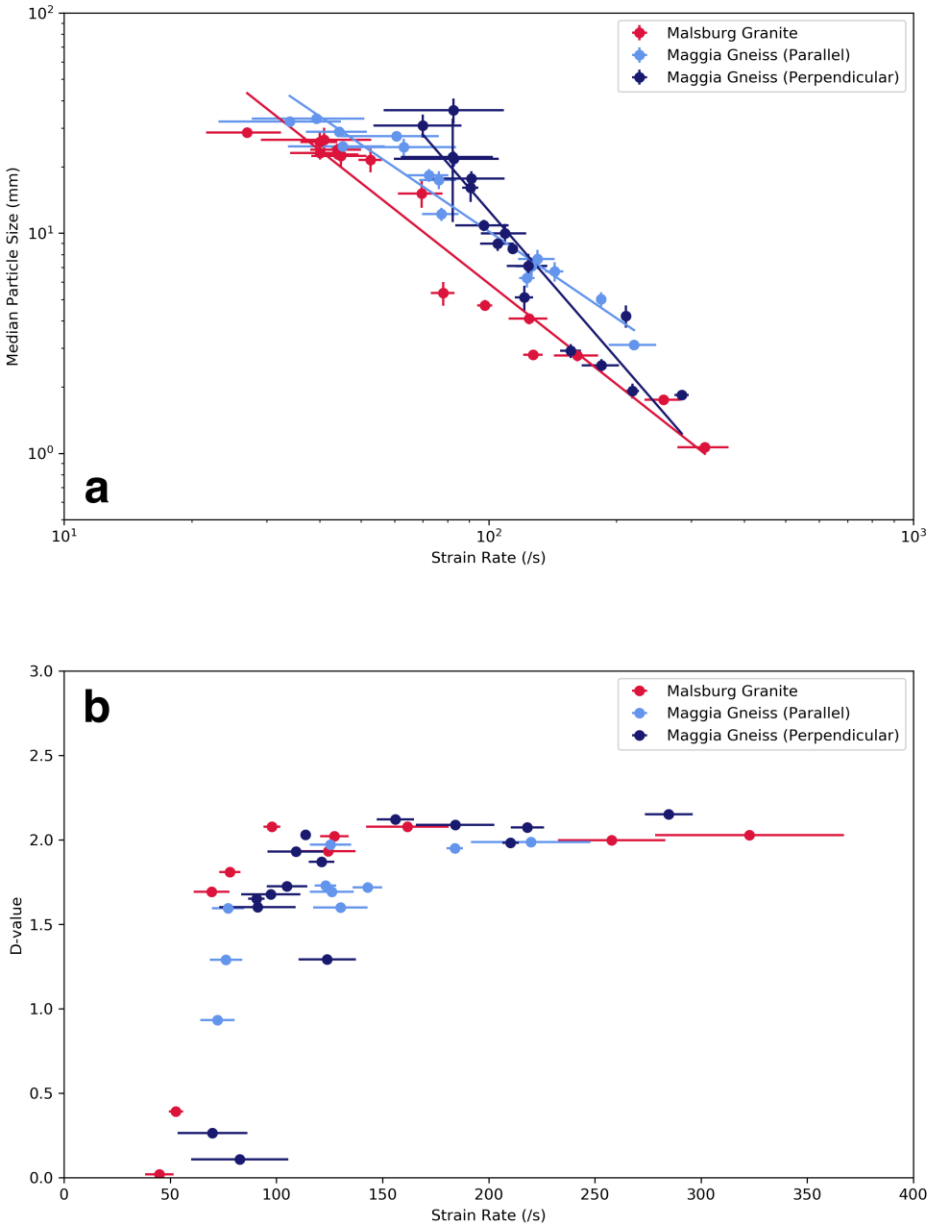

Figure 5. Characteristics of fragment size distributions with varying strain rate: a) median particle size. x- and y- uncertainties are shown for all points where the uncertainty bars are larger than the size of the point. b) D-values of the fragment size distributions, Data presented with a logarithmic x-axis are shown in **Supplementary Figure 4**.

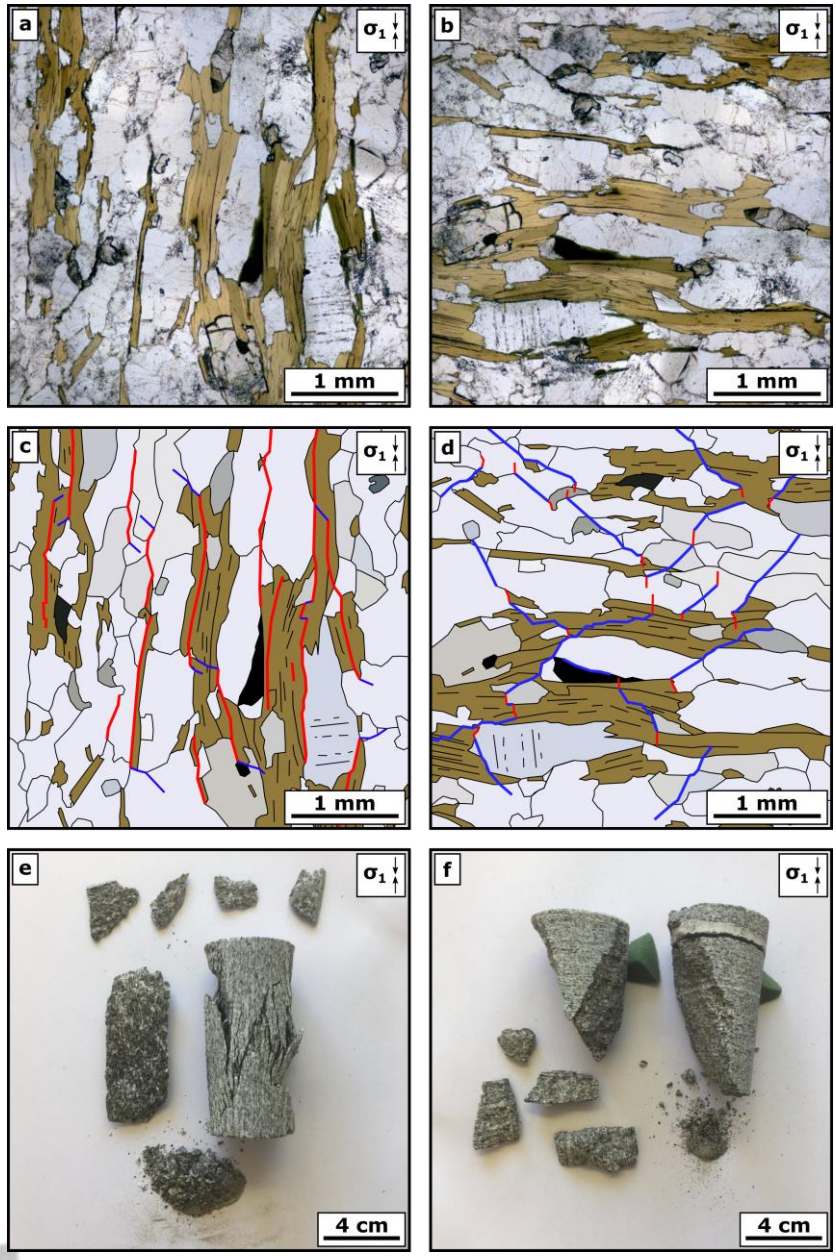

Figure 6. Micro- and macro-scopic deformation of Maggia Gneiss under compression at different orientations. a) and b) Plane polarized optical microscope image of pristine Maggia Gneiss. c) and d) Schematic drawings of the different fracturing styles under compression parallel to and perpendicular to the foliation respectively, red traces illustrate predominantly tensile (Mode I) fractures while blue traces illustrate predominantly shear fractures (Mode II and/or Mode III). e) and f) Fragments resulting from quasi-static compression parallel to and perpendicular to the foliation respectively.

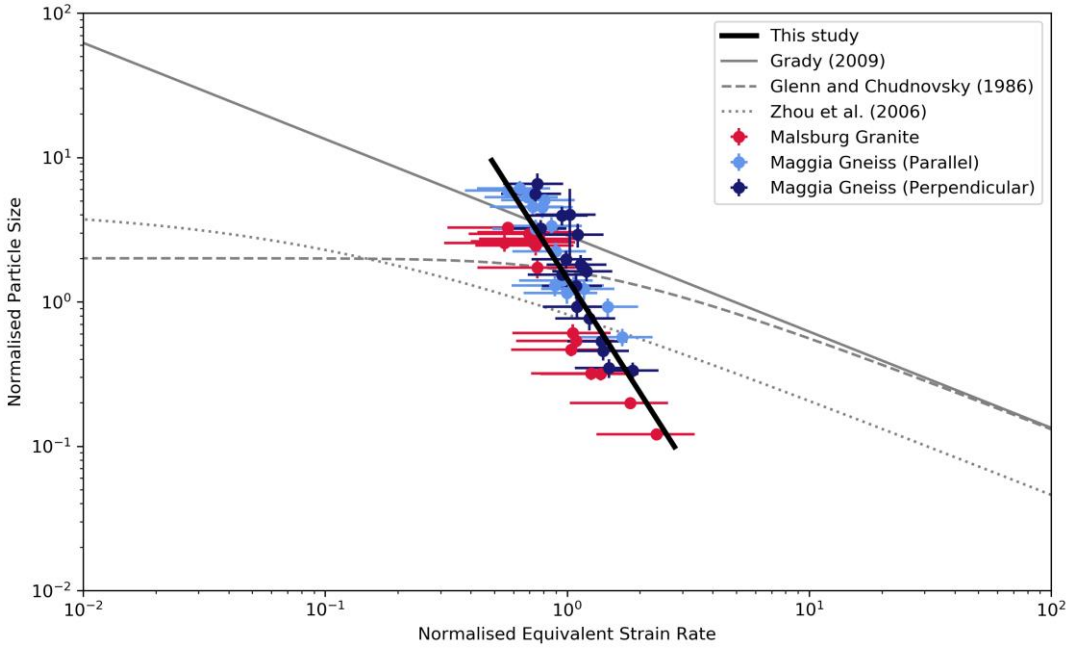

Figure 7. Scaled median fragment size variation with the scaled equivalent tensile strain rate, compared to scaled tensile fragmentation models. The functions of the scaled tensile fragmentation models plotted here are defined in (Hogan et al., 2016).

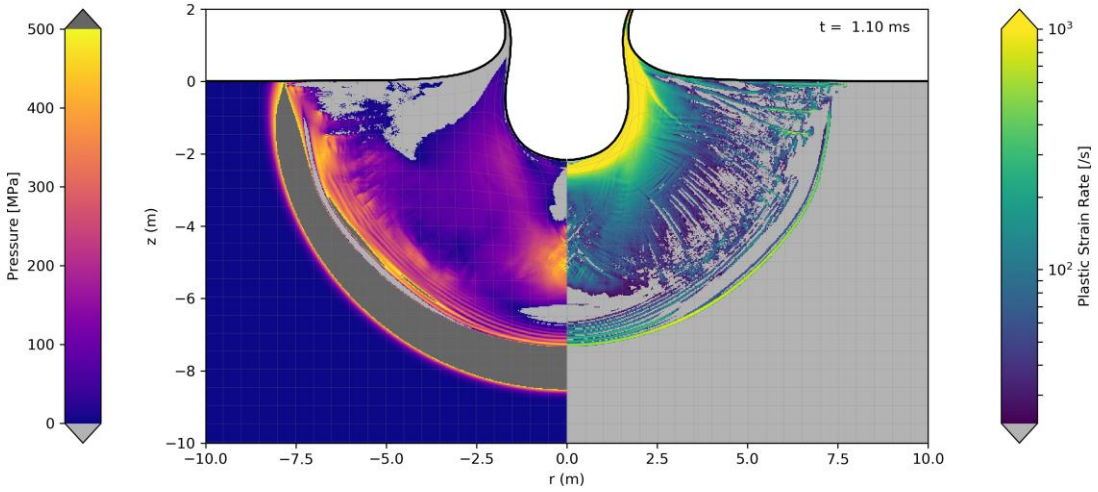

Figure 8. Crater excavation in an iSALE simulation of a 1 m diameter granite sphere impacting at 15 km s^{-1} into a granite target. Left: Colored regions indicate pressures between 0 and 500 MPa, regions of tension are colored light grey while regions of high confining pressure (e.g. within the shock wave) are colored dark grey. Right: Colored regions indicate strain rates greater than 22.9 s^{-1}, regions with lower strain rates are colored light grey. Regions that are colored in both panels are undergoing deformation in a regime where strength and fragmentation should be strongly controlled by strain rate. See **Supplementary Video 1** for conditions from the moment of impact to 4.00 ms.

Table 1. Measured material properties of the Malsburg Granite and Maggia Gneiss.

	Malsburg Granite	*Maggia Gneiss (parallel)*	*Maggia Gneiss (perpendicular)*
E (GPa)	36.1 ± 1.5	39.0 ± 4.4	33.0 ± 2.0
ν	0.224 ± 0.035	0.209 ± 0.027	0.286 ± 0.158
ρ (kg m^{-3})	2623 ± 4	2745 ± 14	
φ (%)	0.29 ± 0.02	0.46 ± 0.01	
σ_0 (MPa)	130.5 ± 14.2	149.5 ± 11.7	181.0 ± 12.8
$\dot{\varepsilon}_0$ (s^{-1})	217 ± 95	234 ± 79	240 ± 67
N	-1.52 ± 0.09	-1.31 ± 0.08	-2.23 ± 0.20
*V_p (m s^{-1})**	3976 ± 134	3996 ± 262	3949 ± 788

E = Quasi-static Elastic Modulus, ν = Quasi-static Poisson's Ratio, ρ = Bulk Density, φ = Porosity, σ_0 = Characteristic Stress (i.e. Quasi-static Uniaxial Compressive Strength), $\dot{\varepsilon}_0$ = Characteristic Strain Rate, N = Power-law exponent of fragment size vs. strain rate, V_p = P-wave velocity. * Calculated from elastic properties, $v_p = \sqrt{\frac{E(1-\nu)}{(1+\nu)(1-2\nu)\rho}}$